Journal of
Materials Chemistry B

PAPER

View Article Online
View Journal | View Issue

Check for updates

Cite this: *J. Mater. Chem. B*, 2024, **12**, 10719

Understanding selective sensing of human serum albumin using a D–π–A probe: a photophysical and computational approach†

Anamika Bandyopadhyay and Anupam Bhattacharya *

Received 6th June 2024,
Accepted 27th August 2024

DOI: 10.1039/d4tb01229a

rsc.li/materials-b

The human serum albumin (HSA) level is a valuable indicator of an individual's health status. Therefore, its detection/estimation can be used to diagnose several diseases. In this work, we have developed a series of donor–π–acceptor probes, which were found to selectively detect HSA over BSA (bovine serum albumin). Among these probes, **A4**, which bears the trifluoroacetyl group, showed the highest selectivity for HSA, with limits of detection and quantification being 1.36 nM and 2.59 nM, respectively. CD spectroscopy of the HSA–**A4** ensemble indicated an increase in the α-helicity of the protein, while the displacement assays revealed the localization of the probe in the hemin site of HSA. The probe works on the principle of excited state intramolecular charge transfer (ICT). Its selectivity was also validated computationally. Docking experiments confirmed the preference of the probe for the hemin binding IB site of HSA, as observed from the fluorescence displacement assay results, and a comparison of docking scores demonstrated the greater preference of **A4** for HSA compared to BSA. Computational experiments also showed a change in preference for HSA amino acid residues exhibited by the excited state of probe **A4** (Tyr161, Met123, Pro118, and Leu115) when compared to its ground state (Arg186 and His146). Hydrophobic interactions dominated the excited state protein–probe ensemble, whereas there was significant involvement of the water bridges along with the hydrophobic interactions in the ground state ensemble. Probe **A4** was also assessed for its practical utility and found to successfully sense HSA in urine at extremely low concentrations. Moreover, the **A4**–HSA ensemble was employed for hemin sensing with a detection limit of 0.23 μM.

Introduction

Human serum albumin (HSA), the most abundant plasma protein in human blood ($\sim 7.5 \times 10^{-4}$ M), has multiple functions in the human body.[1] These functions range from modulating oncotic pressure to transporting endogenous and exogenous compounds, exhibiting antioxidant properties, improving the solubility and lifetime of hydrophobic compounds, and incapacitating certain toxic substances to orchestrate fluid distribution in different body compartments.[1–6] Microalbuminuria is a condition with mildly elevated albumin levels in urine, whereas massive proteinuria is responsible for nephrotic syndrome, leading to edema, hyperlipidemia, neoplasia, and diabetes.[7,8] To avoid detrimental conditions like these, timely detection of HSA becomes necessary.

Structurally speaking, this protein consists of three homologous domains: I, II, and III. Each domain is further fractionated into two subdomains, A and B, consisting of 4 and 6 α-helices, respectively.[1] In clinical practice, HSA is commonly measured using the bromocresol green (BCG) and bromocresol purple (BCP) assays because of the ease of availability.[9] Nevertheless, the drawback of these techniques is their indiscriminate nature. Several reports suggest an overestimation of plasma albumin by the BCG method; likewise, the BCP method is less conclusive in hemodialysis patients. Van de Logt *et al.*, in a recent research study, showed that the BCG method overestimated the plasma and serum albumin concentrations in patients suffering from hypoalbuminemia due to liver cirrhosis, sepsis, or membranous nephropathy.[10] This research highlighted that based on the outcomes of the BCG assay, close to two-thirds of the patients with membranous nephropathy would receive prophylactic anticoagulant therapy, which was unnecessary. This is why efforts are being invested in developing sensors that can determine the albumin concentration in the serum and urine with greater accuracy.

Department of Chemistry, Birla Institute of Technology and Science-Pilani (Hyderabad Campus), Hyderabad-500078, India. E-mail: anupam@hyderabad.bits-pilani.ac.in; Tel: +91-40-66303522

† Electronic supplementary information (ESI) available. See DOI: **https://doi.org/10.1039/d4tb01229a**

The other existing methods of serum albumin quantification, such as immunoassays, colorimetric assays, *etc.*, have several disadvantages associated with them, such as the expensive and time-intensive nature of immunoassays, subjectivity or predilection in color interpretation, and limited specificity and selectivity of colorimetric assays.[11,12]

Fluorescence methods are being explored as an alternative due to their advantages of low cost and real-time detection.[13–23] Most recent reports show a turn-on fluorescence response upon interaction of the probes with one or more pockets of HSA.[14–19] However, many of these probes suffer from problems like short absorption and emission wavelengths, poor sensitivity and selectivity, and partial solubility in water.

We have previously reported a D–A (donor–acceptor) TICT-based probe, NPNF [2-(4-nitrophenyl)naphtho[2,1-*b*]furan], which is HSA selective but with moderate sensitivity and micromolar range detection values.[15] Besides, the emission maximum of NPNF is in the yellow region, which limits its practical application in biological systems. In this work, we wanted to understand the relationship between ICT exhibited by D–π–A systems and their corresponding ability to act as serum albumin probes. Several donor–π–acceptor systems were designed (**A1**–**A4**) by varying the acceptor moieties while keeping the donor moiety constant [Fig. 1]. A π-spacer in the probes, **A1**–**A4**, was introduced to decrease the HOMO–LUMO band gap, thereby facilitating charge transfer. Further lowering of the band gap was ensured by the electron-withdrawing acceptor group. The most electron-withdrawing group ensures the formation of the lowest band gap and aids in charge transfer.[24–30] An ester-containing acceptor was considered due to its well-known cell permeability.[31] On the other hand, the CF_3 group was chosen for its documented hydrogen-bond-accepting and tetrel bond-forming abilities.[32] A better interaction with the hydrophobic pocket of the protein was also anticipated due to the hydrophobic nature and relatively small size of CF_3. Likewise, the CN group is a known bioisostere of the carbonyl group and has been used in numerous pharmaceuticals.[33] A transition was made from donor–acceptor systems to donor–π–acceptor systems to improve their selectivity/sensitivity toward serum albumins.

Materials and methods

Analytical grade reagents and solvents were procured from commercial sources and were used without further purification. 100–200 mesh silica gel was used for column chromatography. A Bruker AV NEO-400 MHz spectrometer was used for ^{1}H NMR (400 MHz), ^{13}C (100 MHz), and ^{19}F NMR measurements. Chemical shifts were reported in ppm, and TMS was used as the internal standard. Spectra of **A1**, **A2**, **A3** and **A4** were recorded in $CDCl_3$. PBS buffer was used as the solvent in all the experiments. Phosphate buffer was used exclusively for CD measurements. A JASCO V-650 spectrophotometer and a Horiba Fluorolog-3 were used for recording absorption and emission spectra. The Horiba DeltaFlex modular fluorescence lifetime system was used to carry out fluorescence lifetime measurements. An Agilent LC-MS/MS Q-TOF 6540 was used to record the mass of the synthesized probes. The pH measurements were performed on an ELICO L1 120 pH meter. Natural amino acids, proteins, and metals used in the study were obtained from various commercial sources.

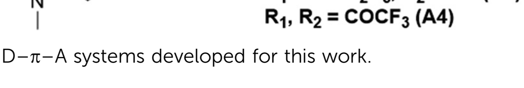

Fig. 1 D–π–A systems developed for this work.

Synthesis of A1, A2 and A3 [Fig. S1, ESI†]

To a solution of (*E*)-3-(4-(dimethylamino)phenyl)acrylaldehyde (2.02 mmol) in EtOH (8 mL) at 25 °C was added the appropriate active methylene compound (2.02 mmol) and piperidine (200 μL). The reaction mixture was allowed to stir at room temperature and checked periodically by TLC. Upon completion of the reaction, the solvent was removed under reduced pressure. The resulting residue was chromatographed on silica gel using various combinations of ethyl acetate/hexanes to obtain the desired compounds.

A1 [diethyl-2-(3-(4-(dimethylamino)phenyl)allylidene)malonate]. Physical appearance: orange crystals.

^{1}H NMR (400 MHz, $CDCl_3$): 1.34 (3H, t, *J* = 8 Hz) 1.41 (3H, t, *J* = 8 Hz), 3.05 (6H, s), 4.28 (2H, q, *J* = 8 Hz), 4.40 (2H, q, *J* = 8 Hz), 6.68 (2H, d, *J* = 8 Hz), 7.01 (1H, d, *J* = 16 Hz), 7.15 (1H, m), 7.42 (2H, d, *J* = 8), 7.58 (1H, d, *J* = 12 Hz).

^{13}C NMR (101 MHz, $CDCl_3$): 165.9, 165.4, 151.5, 147.4, 146.1, 131.4, 129.6, 123.7, 121.1, 118.8, 111.9, 61.0, 40.2, 14.3.

HRMS-ESI(+) *m*/*z*: calculated for $C_{18}H_{24}NO_4^+$ [M + H$^+$]: 318.1705; found: 318.1712.

A2 [ethyl-2-cyano-5-(4-(dimethylamino)phenyl)penta-2,4-dienoate]. Physical appearance: maroon solid.

^{1}H NMR (400 MHz, $CDCl_3$): 1.28 (3H, t, *J* = 8 Hz), 2.98 (6H, s), 4.23 (2H, q, *J* = 8 Hz), 6.58 (2H, d, *J* = 12 Hz), 6.97 (1H, dd, *J* = 14.4 Hz, 12 Hz), 7.08 (1H, d, *J* = 14.8 Hz), 7.39 (2H, *J* = 8 Hz), 7.87 (1H, *J* = 12 Hz).

^{13}C NMR (101 MHz, $CDCl_3$): 163.4, 156.6, 152.5, 150.3, 130.9, 122.6, 118.1, 115.8, 111.9, 99.2, 61.8, 40.1, 14.3.

HRMS-ESI(+) *m*/*z*: calculated for $C_{15}H_{19}N_2O_2^+$ [M + H$^+$]: 271.1447; found: 271.1448.

A3 [2-(3-(4-(dimethylamino)phenyl)allylidene)malononitrile]. Physical appearance: deep red solid.

^{1}H NMR (400 MHz, $CDCl_3$): 3.10 (6H, s), 6.68 (2H, d, *J* = 8 Hz), 7.02 (1H, dd, *J* = 14.2 Hz, 12 Hz), 7.18 (1H, d, *J* = 16 Hz), 7.48 (2H, d, *J* = 12 Hz), 7.51 (1H, d, *J* = 8 Hz).

^{13}C NMR (101 MHz, $CDCl_3$): 160.6, 153.0, 151.6, 131.6, 121.8, 117.3, 115.0, 113.1, 111.9, 40.1.

HRMS-ESI(+) *m*/*z*: calculated for $C_{14}H_{14}N_3^+$ [M + H$^+$]: 224.1188; found: 224.1185.

Synthesis of A4 [Fig. S1, ESI†]

Piperidine and EtOH were not used. Instead, acetic anhydride was used as the solvent under reflux conditions. The rest of the procedure and stoichiometry remained the same.

A4 [3-(3-(4-(dimethylamino)phenyl)allylidene)-1,1,1,5,5,5-hexafluoropentane-2,4-dione]. Physical appearance: deep red-purple crystals.

^{1}H NMR (400 MHz, $CDCl_3$): 3.05 (6H, s), 6.61 (2H, d, J = 12 Hz), 7.14 (1H, dd, J = 14.4 Hz, 12 Hz), 7.31 (1H, d, J = 14.8 Hz), 7.45 (2H, d, J = 8 Hz), 7.68 (1H, d, J = 12 Hz).

^{13}C NMR (101 MHz, $CDCl_3$): 157.2, 156.0, 153.6, 132.5, 122.7, 120.9, 117.9, 117.3, 115.1, 112.0, 40.2.

^{19}F NMR (376 MHz, $CDCl_3$): 70.87 (s), 74.98 (s).

HRMS-ESI(+) m/z: calculated for $C_{16}H_{14}NO_2F_6^+$ [M + H$^+$]: 366.0929, found mass: 366.0929.

Spectral studies

The stock solution of probes **A1** to **A4** (10^{-2} M) was prepared in DMSO. PBS (pH = 7.4, 20 mM) was the solvent for all absorption and emission studies. Stock solutions of metal ions (10^{-2} M), amino acids (10^{-2} M), and proteins (10^{-3} M) were prepared in Milli Q water. The absorption spectra of all four probes were recorded within the range of 250–700 nm. The emission spectra of each probe were recorded in different solvents, amino acids, proteins, and metal ions in a cuvette with a path length of 1 cm and at 25 °C. The excitation wavelength of **A1** was set at 423 nm, and the emission maximum was obtained at 590 nm. Likewise, the excitation wavelengths of **A2**, **A3**, and **A4** were set at 476, 492, and 540 nm, respectively. Their emission maxima were at 592, 587, and 619 nm.

Theoretical calculations

The ground state S_0 geometry of the probes (**A1**–**A4**) was optimized using density functional theory (DFT), the PBE functional, and the 6-31+g(d) basis set. The conductor-like polarizable continuum model (CPCM) was employed to simulate the water environment around these molecules.

The excited state S_1 calculation was conducted only for **A4** using the TD-DFT (time-dependent) method. All these calculations were performed using the Gaussian 09 package.

Fluorescence quantum yield measurements

The quantum yield for **A4** was measured in toluene, PBS, and in the presence of HSA with PBS as solvent. Rhodamine 6G was used as the standard. The quantum yields were calculated using the formula $\varphi_x/\varphi_s = [A_s/A_x][nx^2/ns^2][D_x/D_s]$, where x: sample, s: reference standard, A: optical density value at the wavelength of excitation, n: refractive index of the solvent, and D: area under the fluorescence spectrum recorded.

Calibration curves and detection limit determination

Calibration curves were plotted to estimate HSA using each of the probes. The linear detection of probes: HSA was monitored in the 0 to 5 μM range for **A1** and **A2**. In comparison, linearity was monitored at an even lower concentration of HSA (0 to 0.5 μM) in the cases of **A3** and **A4**. The limit of detection and the limit of quantification were calculated using $3\sigma/S$ and $10\sigma/S$ rules (where σ is the standard deviation of three and ten blank measurements and S stands for the slope of the curve obtained by plotting fluorescence intensity against analyte concentration).

The measured absorbance of **A4** had an optical density value of >0.05 at both the excitation maxima 540 nm (O.D. = 0.18) and emission maxima 619 nm (O.D. = 0.07). So, it was necessary to introduce corrections for the resultant inner filter effects. The corrected fluorescence intensity was obtained using

$$F_{\text{corr}} = F_{\text{obs}}\,\text{antilog}(\text{OD}_{\text{ex}} + \text{OD}_{\text{em}})/2$$

where OD_{ex} = optical density at the excitation wavelength, OD_{em} = optical density at the emission wavelength, F_{obs} = observed fluorescence intensity, and F_{corr} = corrected fluorescence intensity.

Anisotropy measurements

Single-point anisotropy of **A4** and the **A4**–HSA conjugate was measured at an excitation wavelength of 540 nm and an emission wavelength of 619 nm. Each sample was measured ten times, and the results were averaged.

TCSPC data

Fluorescence lifetimes of **A4** and HSA-bound **A4** were determined using TCSPC. The analysis of the decay plots was done using the Horiba EZ time software. χ^2 values were used to determine the goodness of the fit. The average singlet excited state lifetime values for the biexponential decays were calculated using the formula $\langle\tau_f\rangle = \alpha_1\tau_1 + \alpha_2\tau_2$, where $\alpha_1 + \alpha_2 = 1$ and α_1 and α_2 are the relative amplitudes and τ_1 and τ_2 are the lifetimes of the two components.

Establishment of the binding site(s) of A4 in HSA

A4 was dissolved in DMSO to obtain a 10 mM stock solution. Aspirin (subdomain II A), ibuprofen (subdomain III A), and hemin (subdomain IB), which are long-established drugs known to bind to HSA, were selected for the experiment. 10 mM stock solutions of these drugs were made in DMSO. Displacement of **A4** from the **A4**–HSA ensemble was monitored by adding these drugs at increasing concentrations of up to 100 μM.

Circular dichroism

Circular dichroism spectra were recorded in the far-UV region on a JASCO J1500 CD spectrometer equipped with a thermoelectric cell holder at 25 °C and using a cuvette of path length 1 mm. A HSA concentration of 1 μM and ligand concentrations of 2.5 μM, 5 μM, and 7.5 μM were used during the experiments. The scan rate was maintained at 50 nm min^{-1}. The spectral range was 200 to 250 nm, and the ellipticity range was −120 to 200 mdeg. The spectra shown are an average of three consecutive scans. The analysis of the spectra was performed using the BESTSEL application.

Molecular docking

Schrodinger Suite 2022-1 was employed to prepare the crystal structure of the protein obtained from the RCSB PDB, generate a grid, prepare the ligand, and perform molecular docking.

Protein preparation was carried out using the 'protein preparation workflow'. For the protein HSA, the resolutions of the structures obtained from PDB were as follows: 3.2 Å for 1O9X and 2.70 Å for 2I2Z and 2BXG. The following changes were introduced before running the protein preparation. The simulation pH was maintained at 7.4. The protein pre-processing step involved filling in the missing side chains and introducing disulfide bonds wherever appropriate. The option 'optimize H-bond assignments' took care of allotting appropriate orientation of the hydrogen atoms that are part of the protein's amino acids and the water molecules (solvent). It also assigned the correct protonation state to each amino acid in the protein by calculating the pK_a value. The 'clean up' section ensured that the protein was brought to a local energy minimum and also involved removing water molecules that are farther away (beyond 5 Å), as these will not be involved in the protein–ligand interaction.

Grid generation was done to identify the binding pocket in the protein. The application-based tool that was used to generate the grid was Glide. The prepared protein (receptor) had a ligand (*e.g.*, hemin/aspirin/ibuprofen, *etc.*) bound to it. Hence, identifying and removing the existing ligand from the grid was necessary. So, in the 'grid generation panel,' the options 'pick to identify the ligand' and 'show markers' were selected. Ligand selection was done by selecting any one atom of the ligand. Following this, the job was run.

Ligand preparation was the next step, where the .mol file of the ligand **A4** was introduced into the workspace. The 'LigPrep' application was used to prepare the ligand. This application generates the ionization and stereoisomers wherever applicable, and the pH is set to 7.4 ± 0.0 before running the job.

Molecular docking was the final step, where the 'Ligand Docking' application of 'Glide' was used.

For the protein BSA, the resolution of the structure 4F5S obtained from the PDB was 2.47 Å. Protein preparation, grid generation, ligand preparation, and molecular docking were carried out using the same procedure adopted for HSA.

The site score was calculated using the formula: site score = $0.0733\sqrt{n} + 0.6688e - 0.20p$, where n = the number of site points (capped at 100), e = enclosure space, and p = hydrophilic score.

A score greater than 1 suggested a promisingly good site, and a score of 0.8 was used to distinguish a binding site from a non-binding one.

Molecular dynamics simulation and analysis

Molecular dynamics simulation was performed using Desmond to study the **A4**–HSA interaction. The 'System Builder' application in Maestro created the simulation system. The protein 1O9X–ligand **A4** complex was centrally placed in a cubic box 10 Å × 10 Å × 10 Å to create a hydration model. The solvent model chosen to compute and mimic the bulk water properties was the SPC (single point charge) model. Accordingly, the force field applied in the experiment was OPLS4 (optimized potential for liquid simulation) due to its compatibility with the SPC water model. To cater to the negative charge of −13 on the protein (developed due to the different protonation states of the amino acid residues after the protein minimization step), the counter ion +13 Na was added to neutralize the system. A similar procedure was followed for ligand **A4*** (excited state structure obtained using the TD-DFT method). Simulation studies were also performed for the apoprotein 1O9X.

Finally, the molecular dynamics application in Maestro was used to perform simulations. The following parameters were set up before running the simulation: the simulation time was set to 100 ns; the trajectory was recorded at intervals of 10 ps; and the approximate number of frames generated was 10 000. The ensemble class chosen for the experiment was NPT; the temperature was maintained at 300 K, and pressure was set at 1.01325 bar. Maestro's 'System Interaction Diagram' application was used to analyze the MD simulations data.

Calculation of root mean square deviation (RMSD) and root mean square fluctuation (RMSF)

$$\mathrm{RMSD}_x = \sqrt{\frac{1}{N}\sum_{i=1}^{N}\left(r'_i(t_x)\right) - \left(r_i(t_{\mathrm{ref}})\right)^2}$$

where N = the number of atoms in the atom selection, t_{ref} = reference time (the first frame is used as the reference frame, at time $t = 0$), and r' = position of selected atoms in frame x after superimposing it onto the reference frame, where frame x is recorded at time t_x.

RMSD shows to what extent one protein structure differs from another. The extent is calculated by measuring the average distance between the protein atoms. In our experiment, the approximate number of frames monitored during the simulation was 10 000. Each frame was compared to the reference structure (structure at time $t = 0$).

$$\mathrm{RMSF}_i = \sqrt{\frac{1}{T}\sum_{t=1}^{T}\left\langle\left(r'_i(t)\right) - \left(r_i(t_{\mathrm{ref}})\right)^2\right\rangle}$$

where T = trajectory time over which RMSF is calculated, t_{ref} = the reference time, r_i = position of residue i, r_i' = the position of atoms in residue 'i' after superposition on the reference, and $\langle\,\rangle$ = the average square distance taken over the selection of atoms in the residue.

RMSF shows the local changes that occur in the protein structure. It measures the average atomic displacement of atoms in the protein structure. It provides information about the flexibility of the different regions within the protein.

Results and discussion

All synthesized probes were thoroughly characterized, and DFT calculations were performed. Molecular electrostatic potential (MEP) plots were obtained to understand the charge transfer interaction of probe molecules [Fig. 2]. Frontier molecular orbital analysis showed the localization of the HOMO mainly over the *N*,*N*-dimethylamino phenyl moiety and the π-linker. On the other hand, the LUMO was primarily localized on the

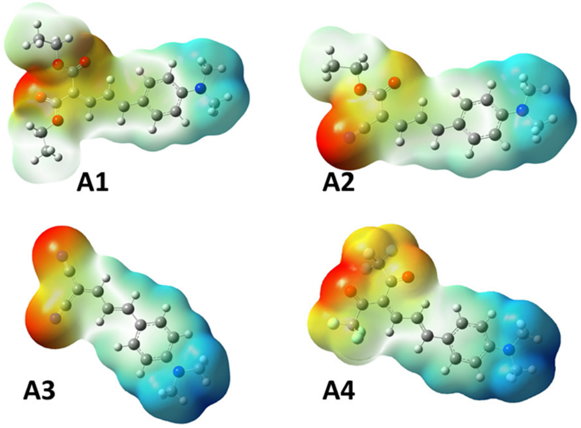

Fig. 2 Electrostatic potential maps of compounds **A1**, **A2**, **A3**, and **A4** obtained using the PBEPBE/6-31+g(d) level of theory: red colour – high electron density region and blue colour – electron deficient region.

electron-withdrawing portion of the compounds, with a marginal extension over the π-bridge [Fig. S15, ESI†]. There was a gradual reduction in the HOMO–LUMO energy gap on moving from probe **A1** to **A4** [Table S2, ESI†].

Photophysical studies of the molecules

Each molecule's absorption and emission spectra were monitored in solvents of different polarities [Table 1 and Tables S3–S5, ESI†]. The absorption spectra showed a double maxima absorption with a higher energy π → π* transition and a lower energy n → π* transition. Upon increasing acceptor strength from **A1** to **A4**, the lower energy n → π* absorption range gradually shifted from a shorter to a longer wavelength range [Fig. S17, ESI†], as articulated computationally [Table S2, ESI†] and experimentally using the Tauc plot [Fig. S16, ESI†].[34,35]

The emission spectrum of the diketo-containing probe **A1** ranged between 450 and 650 nm, whereas that of **A4** ranged from 550 to 700 nm. It was observed that **A1** exhibited positive solvatochromism. The emission maxima shifted bathochromically as we moved from toluene to water. Probe **A4** showed positive solvatochromism when moving from toluene to DMSO. However, the emission maximum in the case of water was slightly hypsochromically shifted [Fig. 3]. The effect of substituents in this series of molecules is perceptible from the shifts obtained in the absorption and emission spectra. In all the cases, the donor and the length of the π bridge remain constant, so the observed redshift in the spectra indicates a stronger intramolecular charge transfer in **A4** compared to **A1**.

Based on the outcome of the preliminary investigations, we decided to monitor the fluorescence behavior of the compounds in solvents of variable polarities. For this experiment, each probe was dissolved in different fractions of THF and PBS. Upon transitioning from THF to PBS, probes **A1** and **A2** exhibited an initial rise in fluorescence intensity followed by a gradual quenching, with emission maxima at PBS : THF (7 : 3) and PBS : THF (4 : 6), respectively. Meanwhile, **A3** was highly emissive in THF and showed a steady drop in fluorescence with an increasing percentage of water. **A4** displayed a similar trend to those of **A1** and **A2** [Fig. S18, ESI†]. Most probes that exhibit AIEE (aggregation-induced emission enhancement) show a drastic fluorescence quenching even in the presence of very little percentage of water, followed by a sudden/gradual emission intensity enhancement, which either continues to rise or fall again.[23,36–38] Unlike these results, all the probes (except **A3**) showed an enhancement in emission upon the introduction of the first aliquot of PBS (PBS : THF ratio of 1 : 9).

A subsequent study focused on the effect of the viscosity changes on the emission intensities of probes [Fig. 4]. An enhancement was observed as the solvent medium was gradually changed from PBS (η = 1.002 mPa s) to glycerol (η = 521.03 mPa s) due to the restriction of intramolecular rotation. These changes were most pronounced in the case of **A4**, where a fluorescence enhancement accompanied by a blue shift of 52 nm was observed upon marginal change in the viscosity (PBS to 10% glycerol–PBS). The possible reason could be stabilizing the locally excited state in the viscous medium.[39,40] In a low-viscosity medium such as water, the intramolecular rotation results in a quick relaxation of the excited state *via* a non-radiative path, which causes a significant lowering of emission. But, in a higher viscosity medium, free rotation is arrested, and the molecules' mode of energy loss is emissive. A low polarity and high viscosity environment is also observed in the hydrophobic pockets of HSA.[39] Given the high sensitivity of **A4** to minute changes in polarity and viscosity, its suitability for HSA sensing was tested upon completion of the preliminary studies.

Studying the behavior of A1–A4 against serum albumins and various analytes of biological importance

Upon completion of the preliminary studies, molecules **A1–A4** were explored for sensing serum albumins, BSA, and HSA.

Table 1 Experimental spectral absorption and emission maxima Stokes shifts and molar extinction coefficient values of **A4** in different solvents

Solvent	Dielectric constant	λ_{nm} (absorbance) for **A4**	ε (M^{-1} cm^{-1})	λ_{nm} (emission) for **A4**	Stokes shift (nm)
Toluene	2.38	525	47 090	599	74
Dioxane	2.25	519	46 830	603	84
THF	7.58	539	44 960	615	76
EtOAc	6.02	528	46 500	611	83
CH_2Cl_2	8.93	544	36 890	614	70
DMF	36.7	567	44 650	629	62
DMSO	46.7	574	57 660	634	60
Water	80.1	515	18 200	623	108

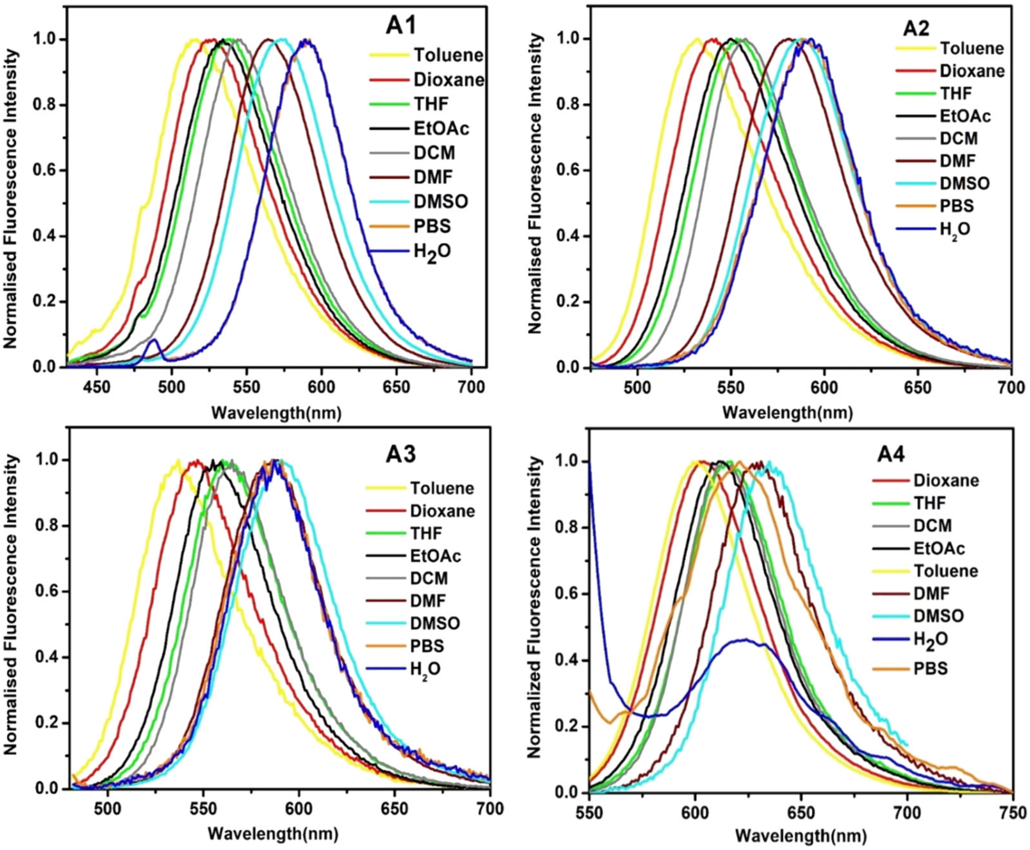

Fig. 3 The emission spectra of **A1**, **A2**, **A3**, and **A4** in solvents of different polarities.

While all the molecules showed fluorescence enhancement when incubated with BSA/HSA, the response towards HSA was better than that towards BSA in all cases [Fig. S19, ESI†]. Compound **A4** gave the best result with ∼182-fold enhancement against HSA, compared to ∼56-fold enhancement against BSA [Fig. 5]. All the other molecules, *i.e.*, **A1**, **A2**, and **A3**, failed to show a clear selectivity for HSA over BSA [Fig. S19, ESI†]. Subsequently, studies were conducted to evaluate the selectivity of these probes against various plausible interferents, such as amino acids, essential cations present in the human body, and proteins of different molecular weights and functions. The studies revealed the retention of selectivity towards serum albumins for all the probes, with **A4** retaining its selectivity despite excess concentration (100 μM) of the competing analytes. While the initial response time of each probe was very low (<30 seconds), it took ∼90 seconds for all the probes to produce a complete emission enhancement [Fig. S24, ESI†].

As previously discussed, the enhancement in the fluorescence intensity of **A4** upon interaction with HSA was due to the polarity and viscosity-sensitive nature of **A4**. The initial non-fluorescence of **A4** in a polar medium like PBS is due to the stabilization of the intramolecular charge transfer state of **A4** *via* the dipole–dipole interaction between the probe and the surrounding media. In contrast, the stability of the ICT state in a non-polar medium, or the hydrophobic pocket of a protein, is significantly lowered. Subsequent stabilization of the locally excited state results in the blue-shifted fluorescence enhancement. Additionally, the restricted motion of the probe inside the protein pocket reduces the non-radiative relaxation significantly, thereby contributing to the turn-on emission.

Given the preference shown by the probes towards HSA, we decided to monitor the changes in the absorption spectra upon interaction with HSA. These measurements showed broad structure-less absorption bands with peak maxima at 416 nm, 475 nm, 490 nm, and 523 nm for **A1**, **A2**, **A3**, and **A4**, respectively [Fig. S20, ESI†]. Upon increasing HSA concentrations, all four probes displayed a bathochromic shift. In the case of **A1** and **A3**, the bathochromic shift was also associated with a mild enhancement in the absorbance value. **A2** and **A4**, on the other hand, exhibited larger bathochromic shifts of 23 nm and 29 nm, along with a lowering of the absorbance values. The accompanying bathochromic shift indicates that the interaction of **A4** with the protein favors a much lower energy absorption. It is important to note that a similar redshift in absorption spectra is reported by amyloid-detecting probes, which showed planarization of the probe molecule with greatly restricted motion.[41]

Finally, fluorescence titration experiments were carried out to quantify the sensitivity of each of these probes toward HSA using limit of detection (LOD) and limit of quantification (LOQ) values [Fig. 6 and Fig. S21–S23, ESI†]. Probes **A1** and **A2** showed a good linear correlation between fluorescence intensity and

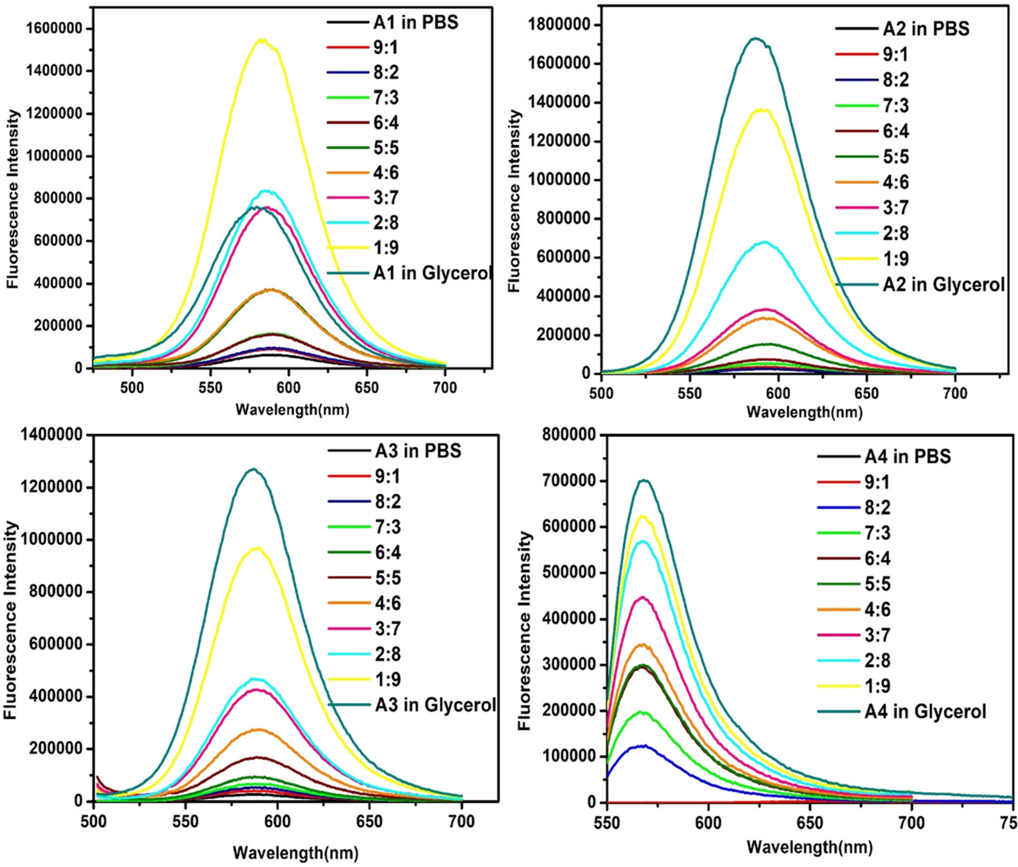

Fig. 4 Fluorescence spectra of **A1**, **A2**, **A3**, and **A4** (10 μM) at different ratios of the glycerol/PBS mixture.

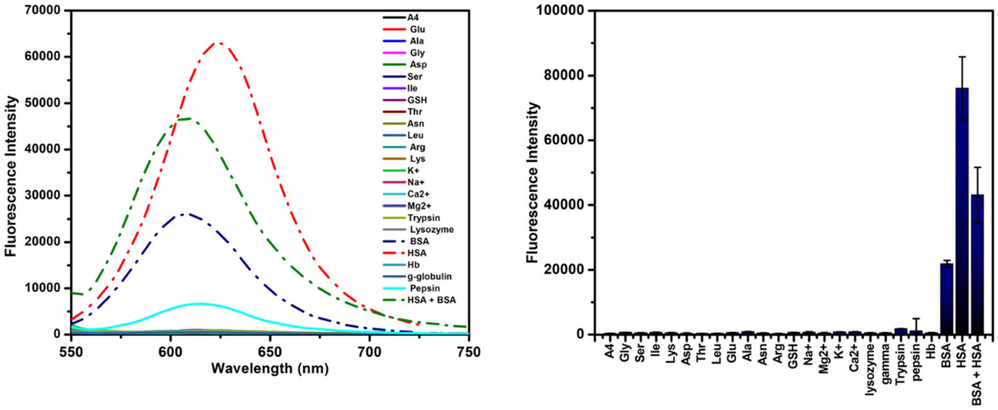

Fig. 5 Fluorescence emission spectra and the corresponding bar plot showing the results of selectivity experiments of **A4** (5 μM) against amino acids/cations (100 μM) and proteins (10 μM). The results were obtained after applying corrections for the inner filter effects.

concentration of HSA (0–5 μM). In the case of **A3** and **A4**, linear detection was possible in the 0 to 0.5 μM concentration range [Fig. S23 and Fig. 6, ESI†]. The LOD and LOQ values were calculated for each probe. **A1**, **A2**, **A3**, and **A4** showed LOD values at 0.128 μM, 0.594 μM, 14 nM, and 1.36 nM, respectively. The LOQ values were 0.55 μM, 7.49 μM, 58 nM, and 2.59 nM for **A1**, **A2**, **A3**, and **A4**, respectively [Table 2]. Lower LOD/LOQ values and an emission wavelength >600 nm prompted us to select **A4** as the preferred probe for further studies. The linearity range in which **A4** detects HSA is 0.0001 g dL^{-1} to 0.02 g dL^{-1}. It is essential to monitor extremely low concentrations of HSA (<0.00365 g dL^{-1}) as such concentrations are associated with in-hospital mortality in acute coronary syndromes (ACS).[42–44]

Before starting further studies, the fluorescence response of **A4** and **A4**–HSA conjugates was also studied at various pH

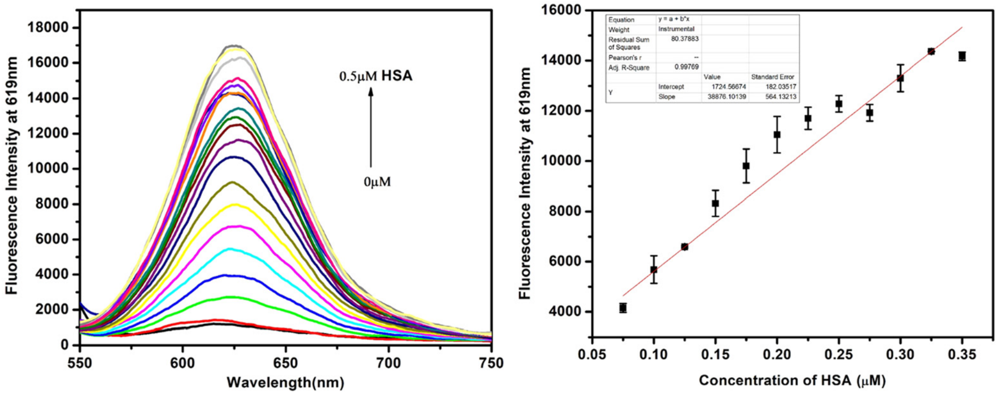

Fig. 6 Fluorescence titration experiment showing the interaction of probe **A4** (5 μM) in the presence of HSA (0 to 0.5 μM) in PBS buffer (pH = 7.4). Calibration curve at λ_{em} = 587 nm for calculating the detection limit for HSA using **A4**.

Table 2 LOD and LOQ values of probes **A1**–**A4**

Probes	LOD	LOQ
A1	0.128 μM	0.55 μM
A2	0.594 μM	7.49 μM
A3	14 nM	58 nM
A4	1.36 nM	2.59 nM

values [Fig. S25, ESI†], revealing an optimal performance at neutral and basic pH (pH 8–9) towards HSA sensing.

Time-resolved fluorescence studies

Time-resolved fluorescence studies were deemed essential to develop an idea about the effect of the immediate environment on the fluorescence lifetime of the probe.[45–48] The free probe **A4** gave a single exponential fitting with a lifetime of 1.01 ns [Table 3 and Fig. S26, ESI†], whereas biexponential fitting was required in the case of **A4**–serum albumin conjugates. In the case of HSA, τ_2 was 1.61 ns with an amplitude (α_2) of ~20%, and τ_1 was 610 ps with an α_1 of ~80%. A similar trend was also observed with BSA, with τ_2 ~1.54 ns and α_2 ~16% and τ_1 ~370 ps and α_1 ~84%. The enhancement of the lifetime of **A4** in the presence of serum albumins can be attributed to the motional restrictions [Table 3], with the associated alpha values indicative of the fraction of the bound probe. In addition, the data also revealed that the lifetime components in HSA are higher when compared to BSA, plausibly due to the localization of the probe in a more hydrophobic region in HSA. Also, a longer lifetime of **A4** in HSA indicated a higher degree of rigidity experienced by **A4**, which causes a slower decay rate to the ground state through a radiative pathway.[49] Upon adding the proteins to the probe, the newly developed component plausibly corresponded to a solvation component as it is ultrafast (on the picosecond scale).

Table 3 Time-correlated single photon count (TCSPC) output of **A4** with and without HSA/BSA

Sample	λ_{max} (nm)	τ_1 (ns)	τ_2 (ns)	τ_{av} (ns)	α_1	α_2	χ^2
A4, 5 μM	619	0.0006	1.01	0.00069	5.41×10^{-20}	1	1.16
A4 + 10 μM HSA	619	0.61	1.61	0.813	0.804	0.195	1.05
A4 + 10 μM BSA	619	0.37	1.53	0.56	0.835	0.164	0.99

Steady-state anisotropy experiments

When the excited fluorophore emits light, it retains some memory of the polarization of the light it absorbed. This feature is exploited while measuring fluorescence anisotropy. Small molecules tumble randomly in solution and get depolarized easily. However, the ease of tumbling depends significantly on the probe's environment. In a viscous medium or a restricted environment, the probe is not free to rotate or tumble; hence, the emission retains the polarization better, and the resultant anisotropy is high. **A4** exhibited near zero anisotropy in the PBS buffer owing to its free rotational movements. Upon addition of the serum albumins, the anisotropy value increased, which indicated the incorporation of the probe in a much-restricted environment of the protein binding pocket(s) [Table 4].

Studies on the changes in the HSA structure upon interaction with A4

It was important to understand if the tertiary structure of the protein had a key role in the enhancement of the emission intensity of **A4**. For this, endopeptidase trypsin was utilized to hydrolyze HSA. It was observed that upon increasing the concentration of trypsin, the fluorescence emission gradually dropped [Fig. S27(a), ESI†]. However, the fluorescence intensity was not entirely quenched. This could possibly be due to **A4** tethering to the hydrophobic environment of the cleaved protein.

In addition, the hydrolysis of the protein was also confirmed by monitoring its emission spectrum. It showed quenching of

Table 4 Anisotropy experiment conducted to evaluate the interaction of **A4** with serum albumins

Ligand/ligand–HSA	Anisotropy	Polarization	Trails
A4 (1 μM)	0.0607	0.08841	10
A4 + HSA (5 μM)	0.1678	0.23222	10
A4 + HSA (10 μM)	0.16779	0.2322	10
A4 (1 μM)	0.10472	0.14926	10
A4 + BSA (5 μM)	0.17546	0.24196	10
A4 + BSA (10 μM)	0.16946	0.23433	10

the tryptophan emission accompanied by a blue shift, which indicated a change in the environment surrounding the lone tryptophan of HSA [Fig. S27(b), ESI†].

The change in intrinsic fluorescence of tryptophan residues within serum albumins was also monitored upon the interaction with **A4**. Quenching of the fluorescence signal was observed in the case of both serum albumins plausibly due to the binding-induced conformational changes or due to changes in the vicinity of the interaction site. The inner filter effect (hence quenching without interaction) was ruled out as **A4** absorbed in the 400 to 600 nm region. In the case of HSA, there are many tyrosines and a lone tryptophan Trp-214. A mild redshift indicated that the tryptophan was exposed to a more polar setting upon such an interaction [Fig. S28(a), ESI†]. A more significant quenching in the case of BSA plausibly originated due to the interaction of the probe with both the surface tryptophan (Trp-134) and the deep-seated tryptophan (Trp-213). No significant change in the polarity was observed upon the interaction of **A4** with BSA [Fig. S28(b), ESI†].

CD spectroscopy was performed to determine the changes in the secondary structure of HSA upon its interaction with **A4**. A pure α-helix conformation generally displays negative bands at 208 nm and 222 nm due to π to π* and n to π* transitions of the nonbonding electrons of the oxygen of the peptide carbonyl in the CD spectra.[50] The spectrum showed an initial decrease in α-helicity, followed by an increase. The overall change in percentage alpha helicity, calculated using BestSel, was from 68% to 70.5% upon treating one equiv. of HSA with 7.5 equiv. of the probe [Fig. 7].

Displacement assays and the recognition mechanism

The displacement assay used three classical drugs: aspirin, ibuprofen, and hemin for sites I, II, and IB, respectively. **A4** was incubated with HSA and then increasing concentrations of site-specific drugs were introduced into this ensemble. When introduced, aspirin and ibuprofen caused minor enhancement in the fluorophore emission [Fig. 8 and Fig. S29, ESI†]. This enhancement was primarily due to the secondary binding of these drugs to their respective binding sites that brought about conformational changes and resulted in the tighter binding of **A4** to HSA.[51] Introduction of hemin, however, led to the complete quenching of the probe's fluorescence at 100 μM, which indicated the binding of the probe to the IB site of the protein.

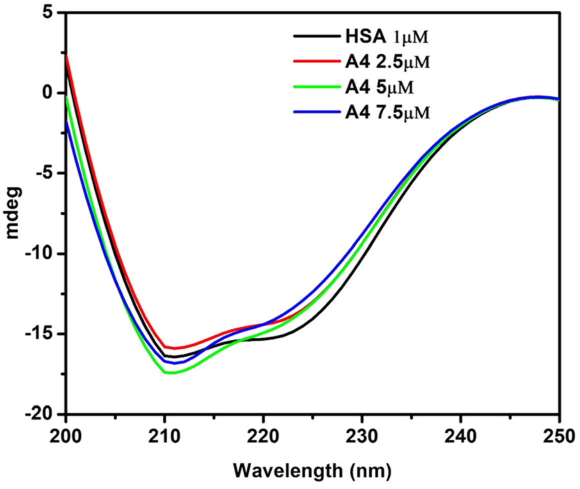

Fig. 7 Circular dichroism spectra of HSA with different molar ratios of **A4** at 298 K. The concentration of HSA was 1 μM in phosphate buffer at pH 7.

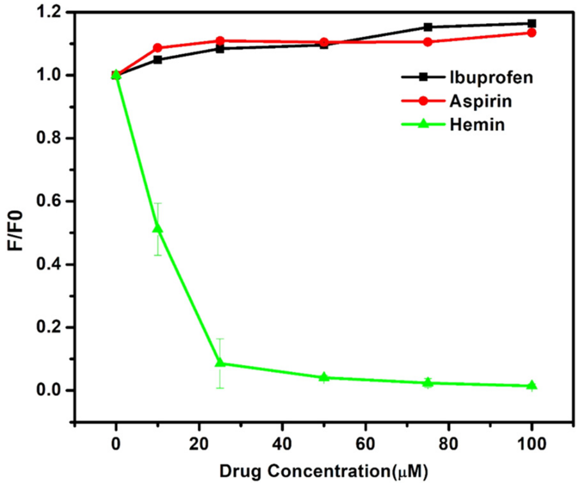

Fig. 8 Displacement assay of **A4** where site-specific drugs were tested against the complex of HSA–**A4**. The expanded version of aspirin and ibuprofen is included in the ESI.†

Molecular docking experiments

After determining the binding site of **A4** using displacement assay, we performed molecular docking to understand the binding interactions between **A4** and HSA at the atomic level. Similar studies were also performed on **A4** and BSA to understand the plausible reason for the difference in the behavior of both serum albumins towards **A4**.

HSA–A4 docking

For appropriate site selection, the following proteins with PDB IDs were chosen: PDB ID: 1O9X for site A (hemin binding site), located in domain IB; PDB ID: 2I2Z for site B (aspirin binding site), located in domain IIA; and PDB ID: 2BXG for sites C and D (ibuprofen binding sites), located in domains III A and II B respectively.

The detailed tabulated report showed the binding affinities of the best-docked poses to be −7.491, −4.90, −6.184, and −5.01 kcal mol^{-1} at sites A, B, C, and D, respectively [Table 5, Fig. 9 and Fig. S30–S32, ESI†]. This indicated that site A, the hemin binding site (IB), was the most preferred binding site, which aligned with the fluorescence displacement assay results.

Determination of most probable binding sites in BSA using 'SiteMap'

The most favorable binding sites in BSA were identified using Schrodinger's 'SiteMap' application [Fig. S33, ESI†]. The Site

Table 5 The gist of the docking calculations at different sites in HSA. The docking score reveals the binding affinity of the best-docked poses in each case

PDB ID	Interacting amino acids	Docking score (kcal mol^{-1})	Types of interactions
1O9X (for site A)	Phe 134, Leu 135, Tyr 138, Met 123, Leu 182, Tyr 1616, Ser 193, Lys 190, Gly 189, Arg 186, Leu 115, Phe 149, Ile 142	−7.491	π–π stacking interactions with Tyr 161, charged interactions (positive) with Lys 190 and Arg 186, polar interactions with Ser 193, and hydrophobic interactions with Tyr 138, Leu 135, Phe 134, Met 123 and Tyr 161
2I2Z (for site B)	Lys 195, Gln 196, Glu 153, Tyr 150, Val 241, Leu 238, Ser 287, Ile 290, Ala 291	−4.90	Polar interactions with Ser 287 and Gln 196, charged (positive) interactions with Arg 257 and Lys 195, charged (negative) interactions with Glu 153, and hydrophobic interactions with Val 241, Leu 238, Tyr 150, Ala 291, Ile 290, Phe 223, and Leu 260
2BXG (for site C)	Leu 430, Leu 453, Val 433, Gly 434, Cys 437, Cys 438, Cys 392, Asn 391, Ile 388, Leu 387, Lys 414, Tyr 411, Arg 410, Leu 407	−6.184	H-bonding interactions with Lys 414 and Arg 410, polar interactions with Ser 489 and Asn 391, hydrophobic interactions with Cys 392, Ile 388, Leu 387, Cys 438, Cys 437, Val 433, Leu 453, Leu 430, Leu 457, Phe 488, Tyr 411 and Leu 407
2BXG (for site D)	Glu 354, Lys 351, Ala 350, Leu 347, Asp 324, Leu 327, Gly 328, Phe 330, Leu 331, Ala 213, Arg 209, Phe 206	−5.01	Charged (negative) interactions with Glu479, Asp 324, and Glu 354, H-bonding interactions with Lys 351, cation–π interactions with Arg 209, polar interactions with Ser 480, and hydrophobic interactions with Leu 481, Leu 347, Ala 350, Phe 206, Ala 210, Ala 213, Leu 331, Phe 330, and Leu 327

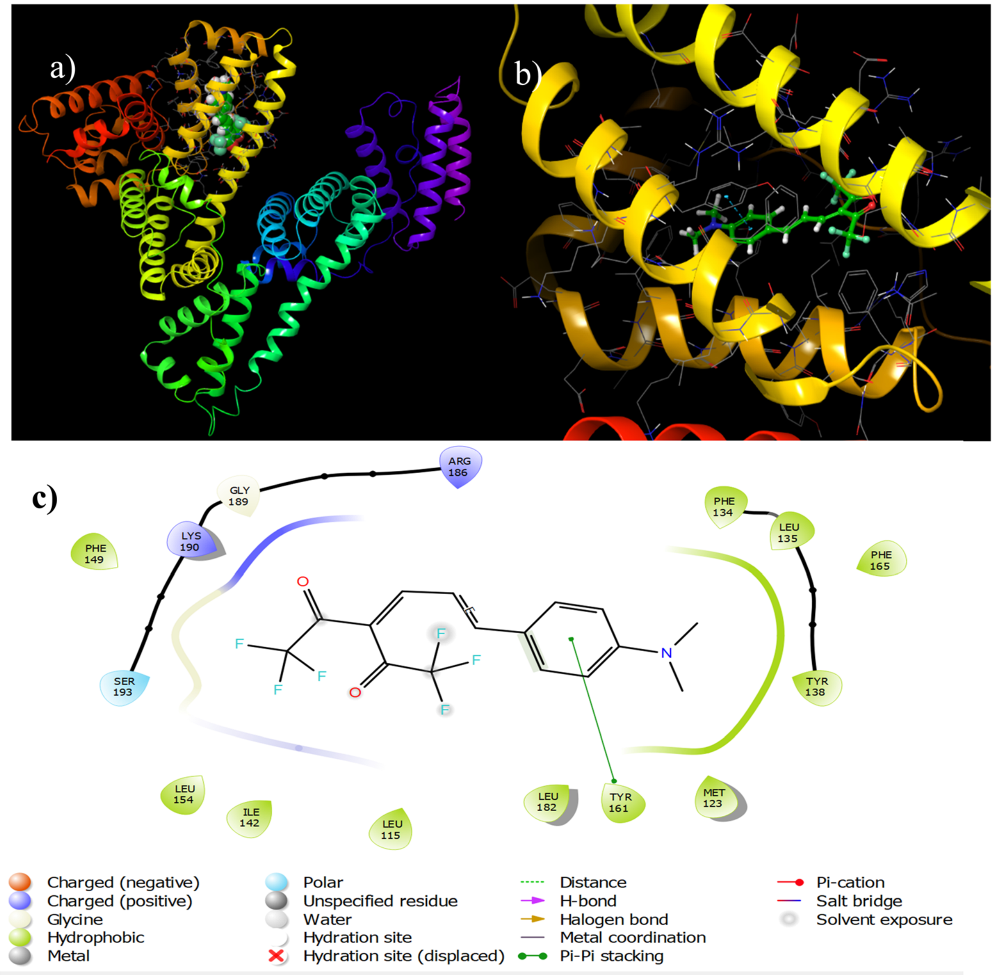

Fig. 9 Binding interactions between **A4** and 1O9X (site A).

Score was used to distinguish the potential sites from the other regions of the protein. Using the 'SiteMap', five different sites were identified with scores of 1.039, 1.063, 1.108, 0.983, and 1.038 for sites 1, 2, 3, 4 and 5, respectively. For BSA–**A4** docking, the scores obtained were −5.399, −4.487, −4.013, −3.211, and −2.333 kcal mol^{-1} for sites 1, 2, 3, 4, and 5, respectively [Table

S10 and Fig. S34–38, ESI†]. This demonstrated that site 1 is the most favorable interaction site and also substantiated the greater binding affinity of **A4** for HSA than BSA.

Molecular dynamics simulations

Although docking provides substantial information about the protein–ligand interaction, it doesn't offer a holistic view of the binding interaction as it assumes a rigid protein structure. On the other hand, molecular dynamics simulates the motion of both the probe and the protein over time, thus revealing a more representative view of the interactions.

Simulation experiments were performed for the apoprotein (only HSA) and the holoprotein [HSA–**A4** (ground state)/HSA–**A4*** (excited state)]. Since the absorption and emission interactions of **A4** with HSA were studied in this work, computationally monitoring the interactions of **A4**/**A4*** with HSA was deemed worthwhile.

Parameters thoroughly studied to understand the **A4**/**A4*** binding to HSA were root mean square deviation (RMSD), root mean square fluctuation (RMSF), protein secondary structure elements (PSSE), and the ligand torsion profile.

Root mean square deviation (RMSD)

RMSD helps quantify the structural similarity between two protein structures, with lower RMSD values indicating greater similarity and higher values implying greater divergence from the original/reference structure. Similar calculations are also performed for the ligand in the protein pocket.

Initially, the RMSD fluctuation of about 5.6 Å units was observed for the apoprotein [Fig. S39, ESI†]. It displayed an increasing trend as the simulation progressed from 0 to 100 ns. However, in the case of the HSA–**A4** conjugate, the protein RMSD (the left *y*-axis in Fig. S40, ESI†) increased in the time frame of 0–20 ns, which subsequently converged beyond 20 ns and led to the RMSD fluctuation in the range of 4.8 Å (Fig. S40, ESI†). Compared to the apoprotein, the decrease in protein RMSD in the case of the HSA–**A4** conjugate indicated stabilization of the protein structure upon interaction with **A4**. Ligand RMSD of the HSA–**A4** interaction initially rose in the 0–20 ns time frame, following which it stabilized and fluctuated around 7 Å. This observation (the right *y*-axis in Fig. S40, ESI†) helps us conceptualize the stability of the ligand in the protein pocket. It is important to note that **A4**, a fairly flexible ligand, has a higher RMSD value compared to the protein by virtue of its immanent conformational freedom. The fluctuations in the ligand structure are possibly due to binding pose variations owing to the conformational changes occurring in the ligand while executing multiple interactions with the amino acid residues during the course of the simulation.

In the case of the HSA–**A4*** ensemble, the protein RMSD rose in the timeframe of 0–10 ns and then fluctuated around 6 Å [Fig. 10]. This indicates a significant difference between the reference structure and the other structures that the protein adopts upon interacting with **A4*** during the simulation. The ligand RMSD shows that **A4*** fluctuates around 6 Å; this closely matches the protein RMSD. Note that the RMSD is lower in the case of the excited state structure of the probe due to its greater rigidity.

Root mean square fluctuation (RMSF)

The protein RMSF plot sheds light on the flexibility/mobility of atoms in the protein structure and helps elucidate the effectiveness of HSA–**A4** and HSA–**A4*** binding and stabilization. The protein residues that interacted with probe **A4** are marked using vertical green lines in Fig. S42 (ESI†). The RMSF value of

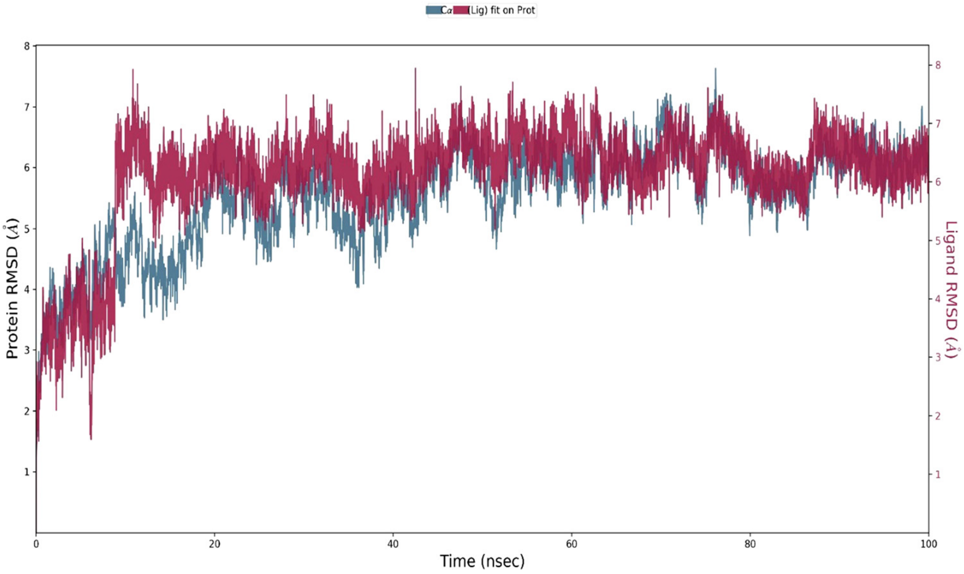

Fig. 10 The RMSD plot obtained for the HSA–**A4*** ensemble. The protein C_α and probe **A4** are shown in blue and red colors, respectively.

HSA residues is lowered when **A4**/**A4*** interacts with the protein [Fig. S41–S43, ESI†]. This reduction in flexibility may be attributed to stabilizing interactions between the ligand and the protein, such as hydrogen bond formation, hydrophobic interactions, or electrostatic interactions.[52]

The ligand RMSF sheds light on the behavior of the ligand within the protein pocket to which it is bound. Both ligand structures **A4** and **A4*** [Fig. S44 and S45, ESI†] showed fluctuations around 2.5 Å; however, it was observed that **A4*** has a lower RMSF than **A4**, which implied an increased rigidity of **A4***.

PSSE analysis

PSSE plots of apoprotein, **A4**, and **A4*** bound protein were monitored during simulation [Fig. S46, ESI†]. The orange-colored bars represent the α-helix. A marginal yet steady rise in the α-helicity (65.26% to 65.52% to 65.90%) was observed as we moved from apoprotein to **A4**–HSA to **A4***–HSA. Noticeably, a similar observation was registered in the CD spectrum, *i.e.*, a marginal rise in α-helix content. This observation may corroborate the lowering of RMSF of the protein upon binding to **A4** and **A4***.

Ligand torsion plot analysis

The ligand torsion profile depicts the conformational evolution of each rotatable bond in the ligand as it moves during simulation. A 2-D structure showing the ligand with different color codes for the single bonds is shown in Fig. 11. The radial plot depicts the conformation of the rotatable bond throughout the simulation. The center of the dial represents the start of the simulation. With the progression of time, the torsion evolution spreads outwards. The bar plot summarises the data of the radial plot by binning the probability density of the torsions from the simulation, thereby providing us with a quantitative picture. The bar plot and the radial plots follow the same color code. The *x*-axis in the bar plot represents the dihedral angles of the ligand, and the *y*-axis represents the ligand population assuming/adopting that particular angle during the simulation. Multiple uniform peaks in the bar plot and the corresponding completely colored radial plot show the ease of free rotation and the subsequent conformations these moieties adopt while interacting with the protein. On the other hand, bonds that exhibit a rather restricted rotation exhibit radial plots colored only in a specific region.

Upon comparing **A4** and **A4*** plots, we see a significant conformational difference in the bond between the phenyl ring and the π linker, depicted in a dark green color. In the case of **A4**, this bond shows a 180° rotation clockwise and counterclockwise [Fig. S47, ESI†], but in the case of **A4***, the rotation/twisting of this bond is restricted severely [Fig. 11]. The torsional potential of **A4*** is lowest in the range of 0 to 60°, as evident from the bar plot. A holistic view of the torsion plots of **A4** and **A4*** shows that the latter adopts and maintains a more rigid structure throughout the simulation. This observation reveals an overall increase in the restriction of motion in **A4*** during its interaction with HSA compared to that observed in the case of **A4**. Owing to this, the intramolecular charge transfer process may be inhibited, which results in the subsequent stabilization and emission from the locally excited state, as observed in the fluorescence experiments.

The simulation data shed light on the stabilizing interactions between the ligand **A4**/**A4*** and HSA, which helped lower the RMSD and RMSF of the protein. Ligand RMSF and ligand

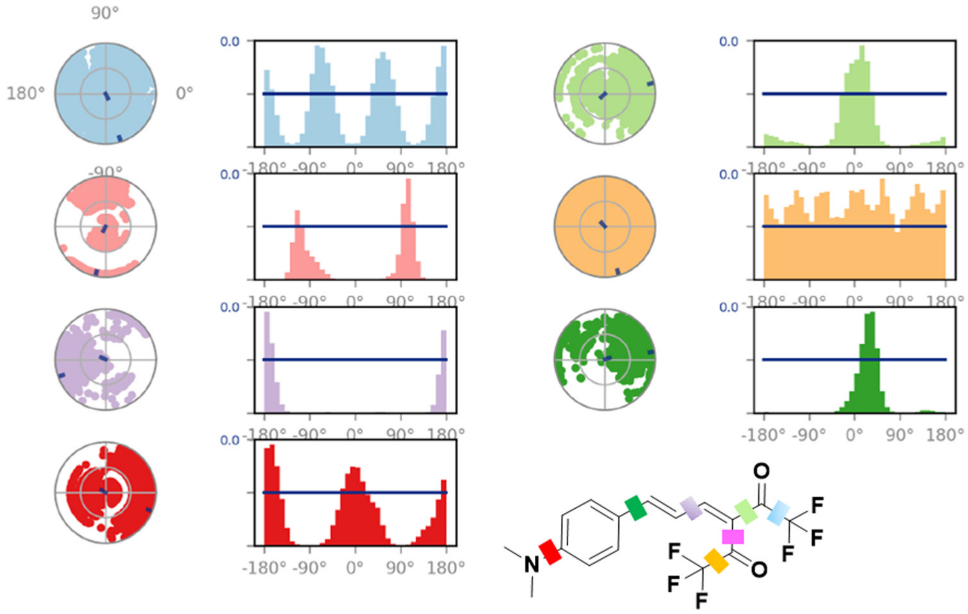

Fig. 11 Torsion plots of the **A4*** ligand inside the protein pocket.

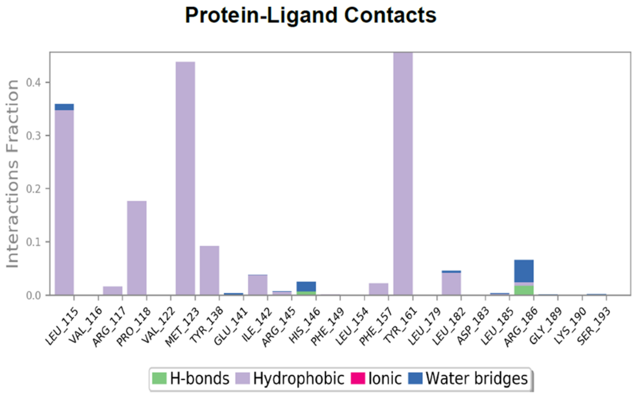

Fig. 12 Histogram representing protein residues interacting with ligand **A4*** in each trajectory frame during the simulation.

torsion plot analyses show a comparatively higher rigidity of **A4*** than that of **A4** in the protein pocket during the course of the simulation. A comparison was made between **A4** and **A4*** interactions with the amino acid residues inside the hemin binding pocket. This showed that the ground state structure **A4** had one strong cation–π interaction with arginine 186 that was persistent throughout the simulation (90% of the time) [Fig. S50, ESI†]. On the other hand, **A4*** showed multiple prominent hydrophobic interactions for a comparatively shorter time span [Fig. 12].

The protein–ligand contact histogram

The HSA–**A4** contacts can be understood from the protein–ligand contact histogram. For the interaction between **A4** and HSA [Fig. S50, ESI†], it was observed that Arg186 and His146 bind to **A4** 90% of the time and 30% of the time, respectively, with minor contributions from Arg145, Ile142, Leu115, and Pro110 [Fig. S50 and S51, ESI†]. The water bridges reflect the interaction between ligand **A4** and HSA mediated by water. These are shown using dark blue labels in the protein–ligand histogram plot. The geometric criteria currently accepted for a ligand–water or a protein–water hydrogen bond are a distance of 2.8 Å between the donor and acceptor atoms (D–H···A), a donor angle ≥110° between the donor–hydrogen–acceptor atoms (D–H···A), and an acceptor angle ≥90° between the hydrogen–acceptor–bonded atom (H–A···B).[53] Water bridges were mainly formed by His146 and Arg186, Leu182 and Ser193. The protein–ligand contact plot showed that Arg186 interacts with the ligand **A4** more or less throughout the simulation time, followed by His146 and Arg145 [Fig. S52, ESI†]. Cation–π interactions were observed between positively charged guanidine nitrogens of Arg186 and Arg145 residues and the phenyl ring of **A4** [Fig. S51a and b, ESI†]. It is well known that cation–π interactions are fairly strong electrostatic interactions, with approximately 1.5–2.5 kcal mol^{-1} energy released during the interaction. The known order of the strength of the interaction between the protein and the ligand is salt bridges > H-bonds/halogen bonds > cation–π > π–π.[54] This study also showed that the C-2 in the imidazole ring of His146 formed a tetrel bond with one of the fluorines in the CF_3 moiety of **A4** [Fig. S51(a), ESI†]. Interestingly, the likelihood of this interaction was hypothesized when the probe structure was initially proposed. The Lig plot also shows the various hydrophobic interactions with the amino acid residues in the vicinity, *i.e.*, Tyr161, Leu182, Leu185, Ile142, Phe157, Phe149, Pro110, and Leu112 [Fig. S51(b), ESI†].

The binding mode of ligand **A4*** differed significantly from that observed for **A4**. Here, the major hydrophobic interactions are shown by Tyr161, Met123, Pro118, and Leu115 [Fig. S53, ESI†]. The water bridges and H-bonding are shown by Arg186 and His146 [Fig. 12 and 13]. In the case of **A4***, it is also important to note the lowered interaction fraction compared to that observed for **A4**. For example, Tyr161, which shows the highest interaction fraction among all the other participating residues, interacts with **A4*** for only close to 50% of the simulation time [Fig. 12].

Quantification of HSA in urine

As discussed initially, the extent of kidney damage can be evaluated from the serum albumin concentration in urine. Most reported probes use extremely diluted urine as the emission wavelength of the probe overlaps with the region where many other biological entities present in the urine tend to autofluoresce. This is mainly observed in the lower wavelength

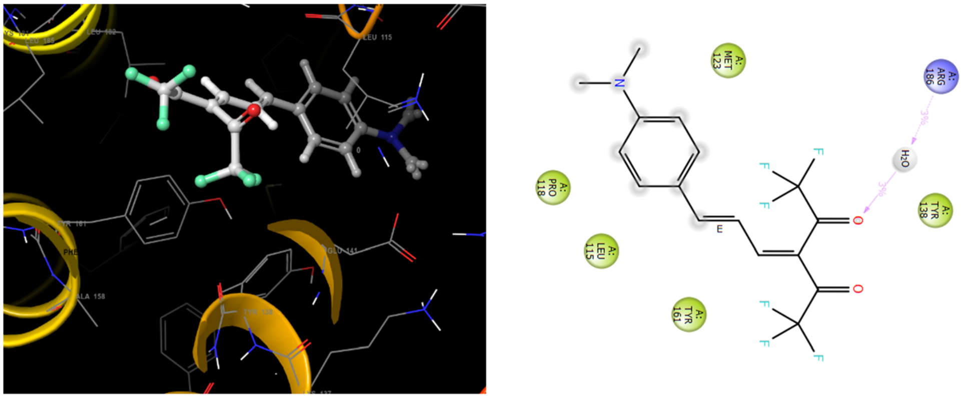

Fig. 13 Snapshot of a trajectory frame showing HSA–**A4*** interaction and its corresponding ligand plot.

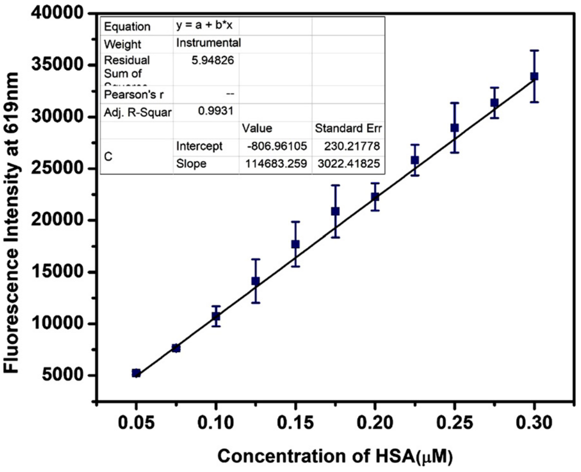

Fig. 14 The change in the emission intensity of **A4** (5 μM) upon the addition of HSA (0 to 0.3 μM) in a 10-fold diluted urine sample in PBS (pH = 7.4).

regions. Considering the probe's ability to sense HSA in the nanomolar range and its near-red emitting ability, we used it to quantify serum albumin in real urine samples. Titration experiments were conducted using real human urine spiked with very low concentrations of HSA ranging between 0.05 and 0.3 μM. The subsequent introduction of **A4** led to a linear rise in the fluorescence intensity of the HSA–**A4** composite [Fig. 14 and Fig. S55, ESI†]. This observation shows the suitability of **A4** to detect and estimate HSA in urine.

Detection of hemin

Hemin, an iron-containing porphyrin compound derived from red blood cells, serves multiple functions, such as regulating ion channels, controlling gene expression, controlling hemoglobin synthesis, and preventing cardiac dysfunction.[55] It also assists as an electron transfer medium due to the reversible redox interconversion of Fe(III)/Fe(II) and is used to treat iron deficiency. The bacteriostatic effects of hemin are also well known.[56–58] Excess of hemin can also have harmful effects, as it oxidizes proteins, nucleic acids, cell membrane components, and lipids and causes cell lysis and death.[59] There are reports on hemin-mediated oxidation of low-density lipids that increase the risk of atherosclerosis.[55]

Several methods for hemin detection have been proposed, including spectroscopic, electrochemical, voltammetric, fluorimetric, and chemiluminescence techniques.[60] Here, we propose hemin detection using the **A4**–HSA ensemble. This proposition is based on the previous displacement assay results where hemin could displace **A4** from its complex with HSA, resulting in a turn-off fluorescence. Before using the **A4**–HSA ensemble, it was necessary to determine the stoichiometry of binding between **A4** and HSA. The fluorescence titration experiment of the probe with HSA showed that the probe binds to the protein in a 1 : 1 ratio [Fig. S56, ESI†]. These results were further corroborated by a linear Stern–Volmer plot and the slope value of the modified Stern–Volmer plot [Fig. S57 and S58, ESI†]. Once the binding stoichiometry was obtained, the 1 : 1 HSA–**A4** complex was used for hemin detection.

Fluorescence quenching of HSA–A4 by gradual addition of hemin

Herein, equal concentrations (5 μM) of HSA and **A4** were mixed in PBS buffer and incubated for 20 minutes, and then emission was recorded. Upon stabilization of the fluorescence signal, hemin was added gradually to this solution up to 10 μM concentration, which resulted in the quenching of the signal [Fig. 15(a) and Fig. S59, ESI†].

Hemin, being the more potent ligand, displaces the weaker ligand **A4** from the binding pocket of HSA. The initial weak ligand (**A4**)–protein (HSA) ensemble is emissive; when the ensemble breaks, the fluorescence gets quenched as **A4** is displaced by hemin. The hemin–HSA complex, on the other hand, is non-emissive in the region where the **A4**–HSA ensemble emits.

A4, when present alone, does not show any quenching or enhancement in its emission signal intensity (**A4** inherently is non-fluorescent in PBS). The fluorescence

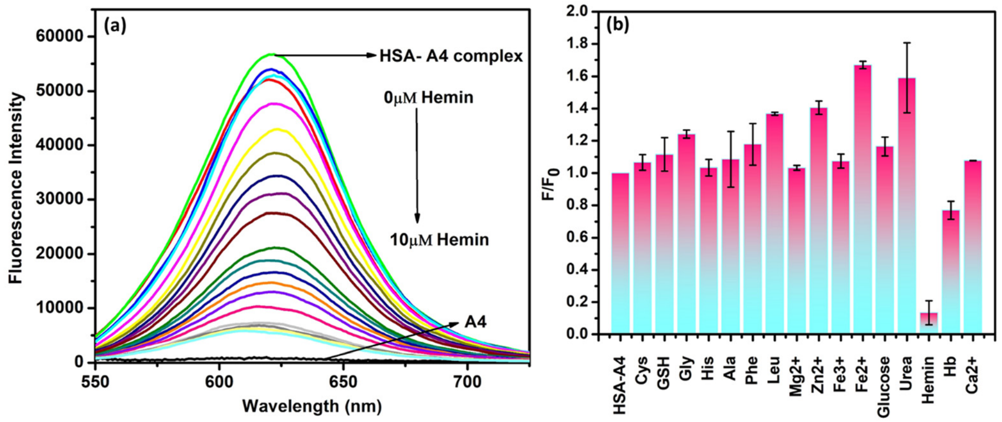

Fig. 15 (a) The fluorescence quenching of the HSA–**A4** ensemble upon incremental addition of hemin. (b) Change in the emission intensity of the **A4**–HSA ensemble upon addition of various cations (100 μM) in PBS (pH 7.4).

intensity (**A4**–HSA–hemin ensemble) was then plotted against the hemin concentration, which exhibited a linear decrease [Fig. S59, ESI†]. It also allowed the calculation of the LOD and LOQ values of 0.23 μM and 0.66 μM, respectively.

The HSA–**A4** ensemble was tested against well-known entities such as amino acids, ions, glucose, urea, and hemoglobin [Fig. 15b]. While a few showed an emission enhancement, none showed quenching of the signal except hemin. Similar experiments were also performed where hemin was introduced into the media containing **A4**–HSA along with the above-mentioned entities. In all the cases, the fluorescence remained quenched except when Fe^{2+} was present [Fig. S60, ESI†]. This result demonstrates the selectivity of HSA–**A4** towards hemin and its suitability for hemin detection in biological systems.

Conclusions

In this work, we have demonstrated the efficacy of an ICT exhibiting D–π–A system, **A4**, for nanomolar detection (1.36 nM) of HSA. The selective site of binding of the probe within HSA was shown *via* displacement assay and was further substantiated by docking studies. Molecular docking experiments also highlighted **A4**'s preference for HSA over BSA. The simulation experiments clearly show the tetrel bond-forming ability of the CF_3 group available in the molecule in accordance with the initial design hypothesis of the probe. The simulation experiments were also conducted using the excited state structure of the ligand, **A4***. These experiments showed that compared to **A4**, **A4*** maintained a more rigid structure throughout the simulation and exhibited greater hydrophobic interactions with the amino acid residues. The probe was applied to detect serum albumin levels in spiked urine samples, and the **A4**–HSA ensemble was used to detect hemin. The limit of detection for hemin was observed to be 0.23 μM. Given the importance of ascertaining serum albumin levels in clinical studies, work is currently undertaken in our lab to structurally modify the developed scaffold to further enhance its sensitivity and selectivity towards HSA.

Data availability

All the data obtained during this study are included in the main manuscript and the ESI† portion of this paper.

Conflicts of interest

There are no conflicts to declare.

Acknowledgements

DST-SERB is acknowledged for the research grant CRG/2022/002175. The authors would like to thank the Central Analytical Laboratory and the high-performance computing facility of the BITS-Pilani Hyderabad campus for helping to obtain the spectroscopic and computational data and Dr Abhijit Kayal, a Senior Scientist from Schrodinger Inc., for constant support with our queries related to the software.

References

1 G. J. Quinlan, G. S. Martin and T. W. Evans, Albumin: biochemical properties and therapeutic potential, *Hepatology*, 2005, **41**(6), 1211.

2 T. R. Guizado, Analysis of the structure and dynamics of human serum albumin, *J. Mol. Model.*, 2014, **20**(10), 2450.

3 G. Fanali, A. di Masi, V. Trezza, M. Marino, M. Fasano and P. Ascenzi, Human serum albumin: from bench to bedside, *Mol. Aspects Med.*, 2012, **33**(3), 209.

4 C. E. Ha and N. V. Bhagavan, Novel insights into the pleiotropic effects of human serum albumin in health and disease, *Biochim. Biophys. Acta*, 2013, **1830**(12), 5486.

5 S. P. Clavant, T. M. Osicka and W. D. Comper, Albuminuria: Its Importance in Disease Detection, *Lab. Med.*, 2007, **38**(1), 35–38.

6 B. K. Paul, N. Ghosh and S. Mukherjee, Interplay of Multiple Interaction Forces: Binding of Norfloxacin to Human Serum Albumin, *J. Phys. Chem. B*, 2015, **119**(41), 13093.

7 M. Bernardi, P. Angeli, J. Claria, R. Moreau, P. Gines, R. Jalan, P. Caraceni, J. Fernandez, A. L. Gerbes, A. J. O'Brien, J. Trebicka, T. Thevenot and V. Arroyo, Albumin in decompensated cirrhosis: new concepts and perspectives, *Gut*, 2020, **69**(6), 1127–1138.

8 J. J. Ho, A. S. Adnan, Y. C. Kueh, N. J. Ambak, H. Van Rostenberghe and F. Jummaat, Human albumin infusion for treating edema in people with nephrotic syndrome, *Cochrane Database Syst. Rev.*, 2019, **7**(7), CD009692.

9 S. Choi, E. Y. Choi, D. J. Kim, J. H. Kim, T. S. Kim and S. W. Oh, A rapid, simple measurement of human albumin in whole blood using a fluorescence immunoassay (I), *Clin. Chim. Acta*, 2004, **339**(1–2), 147.

10 A. E. van de Logt, S. R. Rijpma, C. H. Vink, E. Prudon-Rosmulder, J. F. Wetzels and M. van Berkel, The bias between different albumin assays may affect clinical decision-making, *Kidney Int.*, 2019, **95**(6), 1514–1517.

11 A. Regeniter and W. H. Siede, Peaks and tails: Evaluation of irregularities in capillary serum protein electrophoresis, *Clin. Biochem.*, 2018, **51**, 48–55.

12 M. Lettieri, P. Palladino, S. Scarano and M. Minunni, Protein-templated copper nanoclusters for fluorimetric determination of human serum albumin, *Mikrochim. Acta*, 2021, **188**(4), 116.

13 A. Bandyopadhyay, A. Kumar Shukla, P. Singh, A. Mahale, S. Sharma Irukuvajjula, R. Vadrevu, O. P. Kulkarni, M. Dixit and A. Bhattacharya, Nickel-assisted selective detection of histidine and histidine-rich proteins via an ON-OFF-ON fluorescent probe and its imaging in live cells, *J. Photochem. Photobiol., A*, 2023, 443.

14 X. Liu, S. Qi, J. Mao, Y. Zhang, B. Dong, B. Song and L. Ji, A supramolecular ratiometric fluorescent probe for the detection of human serum albumin, *Dyes Pigm.*, 2024, 224.

15 A. Bandyopadhyay, R. Hazra, D. Roy and A. Bhattacharya, HSA over BSA: Selective detection of Human Serum Albumin via a naphtho [2,1-*b*] furan-based system, *Chem. – Asian J.*, 2024, **19**(5), e202301055.

16 K. P, B. Chakraborty, V. Rani and A. L. Koner, Rationally designed far-red emitting styryl chromones and a magnetic nanoconjugate for strip-based 'on-site' detection of metabolic markers, *J. Mater. Chem. B*, 2022, **10**(26), 5071–5085.

17 Y.-R. Wang, L. Feng, L. Xu, J. Hou, Q. Jin, N. Zhou, Y. Lin, J.-N. Cui and G.-B. Ge, An ultrasensitive and conformation sensitive fluorescent probe for sensing human albumin in complex biological samples, *Sens. Actuators, B*, 2017, **245**, 923–931.

18 H. Xu, G. Shen, C. Peng, X. Han, L. Duan and T. Cheng, BODIPY-based fluorescent probe for selective detection of HSA in urine, *Dyes Pigm.*, 2022, 197.

19 Y. J. Xu, M. M. Su, H. L. Li, Q. X. Liu, C. Xu, Y. S. Yang and H. L. Zhu, A fluorescent sensor for discrimination of HSA from BSA through selectivity evolution, *Anal. Chim. Acta*, 2018, **1043**, 123–131.

20 Z. Huang, H. Wang and W. Yang, Gold Nanoparticle-Based Facile Detection of Human Serum Albumin and Its Application as an INHIBIT Logic Gate, *ACS Appl. Mater. Interfaces*, 2015, **7**(17), 8990.

21 J. Du, Q. Gu, J. Chen, J. Fan and X. Peng, A novel fluorescent probe for the ratiometric recognition of protein based on intramolecular charge transfer, *Sens. Actuators, B*, 2018, **265**, 204–210.

22 H. Li, Q. Yao, J. Fan, J. Du, J. Wang and X. Peng, An NIR fluorescent probe of uric HSA for renal diseases warning, *Dyes Pigm.*, 2016, **133**, 79–85.

23 Y. Tu, Y. Yu, Z. Zhou, S. Xie, B. Yao, S. Guan, B. Situ, Y. Liu, R. T. K. Kwok, J. W. Y. Lam, S. Chen, X. Huang, Z. Zeng and B. Z. Tang, Specific and Quantitative Detection of Albumin in Biological Fluids by Tetrazolate-Functionalized Water-Soluble AIEgens, *ACS Appl. Mater. Interfaces*, 2019, **11**(33), 29619–29629.

24 H. Yanai, Y. Terajima, F. Kleemiss, S. Grabowsky and T. Matsumoto, Reversing the Bond Length Alternation Order in Conjugated Polyenes by Substituent Effects, *Chemistry*, 2023, **29**(15), e202203538.

25 S. Mayarambakam, M. R. Busireddy, K. Sekar and V. J. Rao, Facile synthesis of A-π-D-π-A architecture organic small molecules. Experimental and theoretical investigation of the effect of a π-conjugated spacer, *Asian J. Org. Chem.*, 2023, **12**, 5.

26 S. Namuangruk, K. Sirithip, R. Rattanatwan, T. Keawin, N. Kungwan, T. Sudyodsuk, V. Promarak, Y. Surakhot and S. Jungsuttiwong, Theoretical investigation of the charge-transfer properties in different meso-linked zinc porphyrins for highly efficient dye-sensitized solar cells, *Dalton Trans.*, 2014, **43**(24), 9166.

27 O. Britel, A. Fitri, A. T. Benjelloun, A. Slimi, M. Benzakour and M. McHarfi, Theoretical investigation of the influence of π-spacer on photovoltaic performances in carbazole-based dyes for dye-sensitized solar cells applications, *J. Photochem. Photobiol., A*, 2022, 428.

28 Y. Sekkat, A. Fitri, O. Britel, A. T. Benjelloun, M. Benzakour and M. McHarfi, A theoretical study on the role of the pi-spacer in the thoughtful design of good light-absorbing dyes with phenothiazine for efficient dye-sensitized solar cells (DSSCs), *J. Mol. Model.*, 2023, **30**(1), 5.

29 M. Bourass, A. El Alamy and M. Bouachrine, Structural and photophysical studies of triphenylamine-based nonlinear optical dyes: effects of π-linker moieties on the D-π-A structure, *C. R. Chim*, 2019, **22**(5), 373–385.

30 Y. Chen, X. Wan and G. Long, High Performance Photovoltaic Applications Using Solution-Processed Small Molecules, *Acc. Chem. Res.*, 2013, **46**(11), 2645–2655.

31 V. G. Klein, A. G. Bond, C. Craigon, R. S. Lokey and A. Ciulli, Amide-to-Ester Substitution as a Strategy for Optimizing PROTAC Permeability and Cellular Activity, *J. Med. Chem.*, 2021, **64**(24), 18082–18101.

32 S. Scheiner, Comparison of CH···O, SH···O, Chalcogen, and Tetrel Bonds Formed by Neutral and Cationic Sulfur-Containing Compounds, *J. Phys. Chem. A*, 2015, **119**(34), 9189.

33 F. F. Fleming, L. Yao, P. C. Ravikumar, L. Funk and B. C. Shook, Nitrile-containing pharmaceuticals: efficacious roles of the nitrile pharmacophore, *J. Med. Chem.*, 2010, **53**(22), 7902.

34 K. S. M. Salih, *ChemistryOpen*, 2022, **11**, e202100237.

35 P. Makuła, M. Pacia and W. Macyk, *J. Phys. Chem. Lett.*, 2018, **9**, 6814–6817.

36 A. Ekbote, S. H. Han, T. Jadhav, S. M. Mobin, J. Y. Lee and R. Misra, Stimuli responsive AIE active positional isomers of phenanthroimidazole as non-doped emitters in OLEDs, *J. Mater. Chem. C*, 2018, **6**(8), 2077–2087.

37 L. Li, R. Wang, L. Wang and L. Huang, Development of phenothiazine-based fluorescent probe with aggregation induced emission (AIE) for detection of hydrazine and its application in imaging of living cells, *J. Mol. Struct.*, 2022, 1249.

38 K. S. Jagadhane, S. R. Bhosale, D. B. Gunjal, O. S. Nille, G. B. Kolekar, S. S. Kolekar, T. D. Dongale and P. V. Anbhule, Tetraphenylethene-Based Fluorescent Chemosensor with Mechanochromic and Aggregation-Induced Emission (AIE) Properties for the Selective and Sensitive Detection of Hg(2+) and Ag(+) Ions in Aqueous Media: Application to Environmental Analysis, *ACS Omega*, 2022, **7**(39), 34888–34900.

39 S. Pei, J. Li, N. Kang, G. Zhang, B. Zhang, C. Zhang and S. Shuang, Synthesis of a new environment-sensitive fluorescent probe based on TICT and application for detection of human serum albumin and specific lipid droplets imaging, *Anal. Chim. Acta*, 2022, **1190**, 339267.

40 S. Pei, J. Li, C. Zhang, G. Zhang, Y. Zhou, L. Fan, W. Wang, S. Shuang and C. Dong, TICT-Based Microenvironment-Sensitive Probe with Turn-on Red Emission for Human Serum Albumin Detection and for Targeting Lipid Droplet Imaging, *ACS Biomater. Sci. Eng.*, 2022, **8**(1), 253–260.

41 G. Kuang, N. A. Murugan, Y. Zhou, A. Nordberg and H. Ågren, Computational Insight into the Binding Profile

of the Second-Generation PET Tracer PI2620 with Tau Fibrils, *ACS Chem. Neurosci.*, 2020, **11**(6), 900–908.

42 E. Gremese, D. Bruno, V. Varriano, S. Perniola, L. Petricca and G. Ferraccioli, *J. Clin. Med.*, 2023, 12.

43 J. Fan, W. Sun, Z. Wang, X. Peng, Y. Li and J. Cao, *Chem. Commun.*, 2014, **50**, 9573–9576.

44 A. Kurtul, S. N. Murat, M. Yarlioglues, M. Duran, A. H. Ocek, C. Koseoglu, I. E. Celık, A. Kilic and O. Aksoy, *Angiology*, 2016, **67**, 34–40.

45 B. K. Paul, N. Ghosh and S. Mukherjee, Interplay of Multiple Interaction Forces: Binding of Norfloxacin to Human Serum Albumin, *J. Phys. Chem. B*, 2015, **119**(41), 13093–13102.

46 A. Albini and S. Monti, Photophysics and photochemistry of fluoroquinolones, *Chem. Soc. Rev.*, 2003, **32**(4), 238–250.

47 M. Y. Berezin and S. Achilefu, Fluorescence Lifetime Measurements and Biological Imaging, *Chem. Rev.*, 2010, **110**(5), 2641–2684.

48 D. De and A. Datta, Unique Effects of Aerosol OT Lamellar Structures on the Dynamics of Guest Molecules, *Langmuir*, 2013, **29**(25), 7709–7714.

49 D. Sarkar, A. Mahata, P. Das, A. Girigoswami, D. Ghosh and N. Chattopadhyay, Deciphering the perturbation of serum albumins by a ketocyanine dye: A spectroscopic approach, *J. Photochem. Photobiol., B*, 2009, **96**(2), 136–143.

50 B. Ranjbar and P. Gill, Circular dichroism techniques: biomolecular and nanostructural analyses- a review, *Chem. Biol. Drug Des.*, 2009, **74**(2), 101.

51 R. Choudhury, A. K. Sharma, P. Paudel, P. Wilson and A. B. Pereira, In situ generation of a Zwitterionic fluorescent probe for detection of human serum albumin protein, *Anal. Biochem.*, 2022, **646**, 114630.

52 H. Maity, M. Maity, M. M. G. Krishna, L. Mayne and S. W. Englander, Protein folding: The stepwise assembly of foldon units, *Proc. Natl. Acad. Sci. U. S. A.*, 2005, **102**(13), 4741–4746.

53 S. Beura and P. Chetti, In-silico strategies for probing chloroquine based inhibitors against SARS-CoV-2, *J. Biomol. Struct. Dyn.*, 2021, **39**(10), 3747–3759.

54 D. A. Dougherty, The cation-pi interaction, *Acc. Chem. Res.*, 2013, **46**(4), 885.

55 T. H. Fereja, S. A. Kitte, W. Gao, F. Yuan, D. Snizhko, L. Qi, A. Nsabimana, Z. Liu and G. Xu, Artesunate-luminol chemiluminescence system for the detection of hemin, *Talanta*, 2019, **204**, 379–385.

56 Y. Lin, M. Li, L. Huang, W. Shen and Y. Ren, Involvement of heme oxygenase-1 in β-cyclodextrin–hemin complex-induced cucumber adventitious rooting process, *Plant Cell Rep.*, 2012, **31**(9), 1563–1572.

57 B. Panijpan, C. Mohan Rao and D. Balasubramanian, Interaction of antimalarial drugs with hemin, *Biosci. Rep.*, 1983, **3**(12), 1113–1117.

58 J. M. Combrinck, T. E. Mabotha, K. K. Ncokazi, M. A. Ambele, D. Taylor, P. J. Smith, H. C. Hoppe and T. J. Egan, Insights into the Role of Heme in the Mechanism of Action of Antimalarials, *ACS Chem. Biol.*, 2013, **8**(1), 133–137.

59 Z. Guo, B. Li, Y. Zhang, Q. Zhao, J. Zhao, L. Li, L. Feng, M. Wang, X. Meng and G. Zuo, Acid-treated Graphitic Carbon Nitride Nanosheets as Fluorescence Probe for Detection of Hemin, *ChemistrySelect*, 2019, **4**(28), 8178–8182.

60 L. Zhao, F. Chen, W. Huang, H. Bao, Y. Hu, X.-A. Huang, T. Deng and F. Liu, A fluorescence turn-on assay for simple and sensitive determination of hemin and blood stains, *Sens. Actuators, B*, 2020, 304.